Maeda and Watanabe
Earth, Planets and Space (2023) 75:115
https://doi.org/10.1186/s40623-023-01870-z

Earth, Planets and Space

FULL PAPER

Open Access

Seismic structure and its implication on the hydrothermal system beneath Mt. Ontake, central Japan

Yuta Maeda[1*] and Toshiki Watanabe[1]

Abstract

Mt. Ontake is an active volcano in central Japan where phreatic eruption activity is prominent. A shallow subsurface structure in the summit region of this volcano has been scarcely studied despite its importance. Our study examines the structure from three seismic analyses: a typical P-wave velocity from the semblance of the vertical propagation of intermediate-depth earthquakes (IDEs), a layered velocity model from P- and S-wave arrival times of shallow volcanic earthquakes, and a pseudoreflection profile from the autocorrelation functions of the IDEs. Our results consistently indicate the presence of three layers, which are interpreted as younger (> 0.1 Ma) and older (0.39–0.78 Ma) eruptive deposits and the basement. A comparison of the structure with hypocentres and deformation sources suggests fluid migration controlled by the structure.

Keywords P-wave velocity, Reflection imaging, Hydrothermal system, Fluid migration

Graphical Abstract

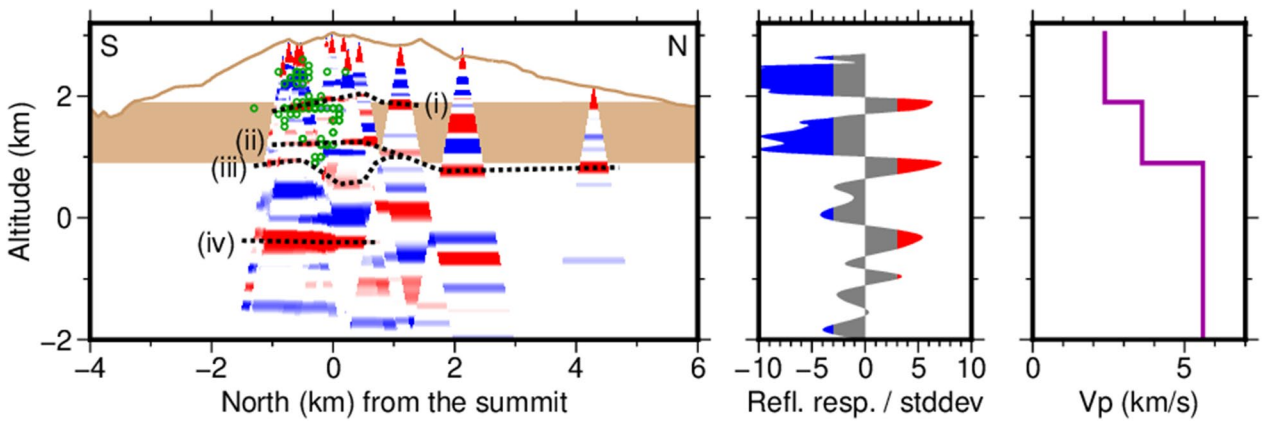

*Correspondence:
Yuta Maeda
maeda@seis.nagoya-u.ac.jp
Full list of author information is available at the end of the article

Introduction

Phreatic eruptions of volcanoes do not involve juvenile materials but are hazardous to near-crater regions, as they sometimes occur without clear precursors (e.g. Christenson et al. 2010; Maeda et al. 2015a; Dempsey et al. 2020; Terada et al. 2021). Our understanding of the mechanisms of phreatic eruptions is not sufficient, although it is rapidly growing owing to recent geophysical or multidisciplinary studies: examples include Tongariro, New Zealand, in 2012 (Jolly et al. 2014); Kverkfjoll, Iceland, in 2013 (Montanaro et al. 2016); Merapi, Indonesia, in 2014 (Metaxian et al. 2020); Hakone, Japan, in 2015 (Mannen et al. 2019); and Lascar, Chile, in 2015 (Gaete et al. 2020). Subsurface structural surveys by electromagnetic (e.g. Miller et al. 2018; Tsukamoto et al. 2018) or seismic (e.g. Wu et al. 2017; Yukutake et al. 2021) approaches have also been conducted at several volcanic fields where hydrothermal activities are dominant. Stix and de Moor (2018) proposed conceptual models for two end members of phreatic eruptions (overpressurization of a relatively deep, sealed hydrothermal system or vaporization of liquid water in a relatively shallow, open hydrothermal system caused by magmatic gas supplies) from case studies at six volcanoes. These studies show recent progress in our understanding of the mechanisms of phreatic eruptions.

Mt. Ontake, central Japan, is an active volcano located behind the volcanic front developed by the subduction of the Pacific plate. The edifice comprised older (0.78–0.39 Ma) and younger (< 0.1 Ma) eruptive deposits (OED and YED, respectively) which cover the surface of this volcano (e.g. Oikawa et al. 2016). The YED–OED boundary (Y–O boundary) is close to or lower than a topography contour of 1.9 km above sea level (asl.) in most directions (Fig. 1a). Asai et al. (2006) proposed an underground water flow along the Y–O boundary based

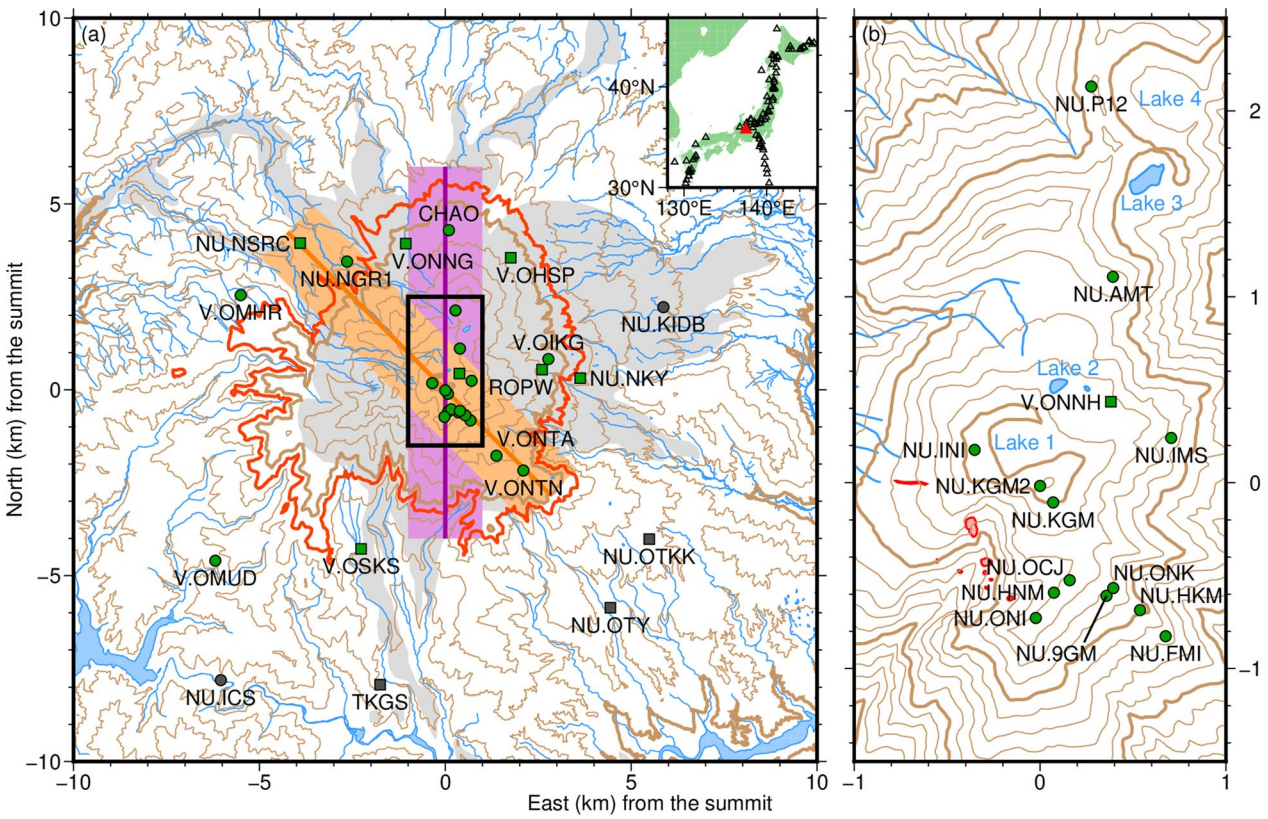

Fig. 1 Seismometer network around Mt. Ontake. Circles and squares are short-period and broadband seismometers, respectively. Green colours show the stations used in the analysis 1. Stations starting with "NU." and "V." are maintained by Nagoya University and the Japan Meteorological Agency, respectively; the other stations are maintained by Nagano and Gifu Prefectures. Blue colours are the lakes and rivers from digital map data from the Geospatial Information Authority of Japan (GSI). **a** Map of a 20 km × 20 km area centred on the summit of Mt. Ontake. Orange and purple colours show the transects used for Fig. 7. Brown contours indicate the topography at 0.2 km intervals. The red line shows a topography contour at 1.9 km asl. The grey area shows the surface covered by the younger eruptive deposits (YED). The inset indicates the locations of the Japanese active volcanoes (black) and Mt. Ontake (red). **b** Enlarged map of the area shown by the black rectangle in **a**. The contour interval is 0.05 km. The red outlines are the locations of 2014 eruptive craters from the GSI

on the spatial distribution of water discharge rates. Mt. Ontake has a ridge with several crater lakes along the north–south (N–S) direction, and the summit is at the southern end of the ridge (Fig. 1b). Recent activities, including the phreatic eruptions in 1979, 1991, 2007, and 2014, occurred from the southwestern flank (Fig. 1b; Kaneko et al. 2016).

Studies on the seismic and geodetic activities of Mt. Ontake have been relatively abundant. Nakamichi et al. (2009) analysed increased seismicity associated with crustal deformation during the 3 months before the 2007 eruption. Kato et al. (2015) and Terakawa et al. (2016) analysed intense seismicity from a month before to several months after the 2014 eruption. Maeda et al. (2015b, 2017) and Ogiso et al. (2015) analysed seismic signals immediately before the onset of the 2014 eruption. Takagi and Onizawa (2016), Murase et al. (2016), and Miyaoka and Takagi (2016) analysed crustal deformations over the periods encompassing the 2007 and 2014 eruptions. Narita and Murakami (2018) and Narita et al. (2019) analysed long-term posteruptive deflation after 2014. Geochemical (e.g. Sano et al. 2015) and petrological (e.g. Ikehata and Maruoka 2016; Maeno et al. 2016; Miyagi et al. 2020) studies on the 2014 eruption have also been conducted.

Compared to these studies on volcanic activities or related temporal changes in observables, studies on the subsurface structure of Mt. Ontake have been limited. Several structural surveys at regional (> 100 km) scales in central Japan (e.g. Ikami et al. 1986; Hirahara et al. 1989; Nakajima and Hasegawa 2007; Hirose et al. 2008) consisted of the Ontake region but did not pay particular attention to Mt. Ontake. Structural surveys at local scales (e.g. Hirahara et al. 1992; Ikami et al. 1992; Inamori et al. 1992; Kosuga 1992; Doi et al. 2013; Ichihara et al. 2018) focused on a seismogenic region to the southeast of the summit. Regarding the subsurface structure of a shallow (1–2 km depth) part beneath the summit, an airborne electromagnetic survey by Abd Allar and Mogi (2016) has been the only published research. Even a typical P-wave velocity in the summit region has not been known, which has prevented the determination of the absolute hypocentre depths of the shallow volcanic earthquakes (SVEs). A reliable P-wave velocity model, even if it is one-dimensional (1-D), can provide a basis to obtain a better understanding this volcano.

A trial seismic observation in the summit region of Mt. Ontake started in November 2017 (Horikawa et al. 2017) and has continued over several years. The data from this observation were exceptional, both in its time length and spatial density, compared to all previous seismic observations in the summit region of this volcano. A structural survey in the summit region was enabled for the first time owing to this data.

In this study, we investigated a shallow subsurface structure beneath the summit region of Mt. Ontake. We did not investigate a detailed three-dimensional (3-D) model because its reliability could be affected by localized spatial distributions of hypocentres and stations at Mt. Ontake. Instead, this study aimed at a reliable and stable estimation of a 1-D model by selecting data and free parameters. Our results provided a basis for the interpretation of phenomena related to fluid migration in a shallow part of this volcano and for better analyses of the seismic data.

Data and methods

Data

We used a seismometer network around Mt. Ontake (Fig. 1) maintained by Nagoya University, the Japan Meteorological Agency (JMA), and the Nagano and Gifu Prefectures. All data were sampled at 100 Hz and telemetered to Nagoya University. We used data from November 1, 2017, when the trial observation in the summit region (green circles in Fig. 1b; Horikawa et al. 2017) started, to the end of 2021.

The seismicity around Mt. Ontake is spatially separated into three groups (Fig. 2): SVEs beneath the summit region, local tectonic earthquakes (LTEs) in the surrounding region, and intermediate-depth (~ 250 km) earthquakes (IDEs) along the subducted Pacific plate. We used the P- and S-wave arrival times of the SVEs and the vertical waveforms of the IDEs.

Routine seismicity monitoring by Nagoya University did not use data from the summit trial stations due to the delay in data transmission. Therefore, small SVEs in the summit region could potentially be missed in the earthquake catalogue created by the routine monitoring (a routine catalogue). To make a more complete SVE catalogue, we detected the SVEs independently of the routine catalogue using all continuous waveforms around Mt. Ontake including the summit trial stations. We used the WIN system (Urabe and Tsukada 1992) for automatic event detection and initial location. This system used the ratios of short- to long-term averages at multiple stations for the event detection and an autoregression algorithm for automatic picking of P- and S-wave arrival times. The initial hypocenters were estimated using these arrival times with the hypocenter determination algorithm proposed by Hirata and Matsu'ura (1987). We regarded the earthquakes that fell in the cylindrical region marked by the black lines in Fig. 2a as SVEs. The results were 1542 SVEs, approximately four times more than the 393 SVEs in the routine catalogue. We manually picked the P- and S-wave

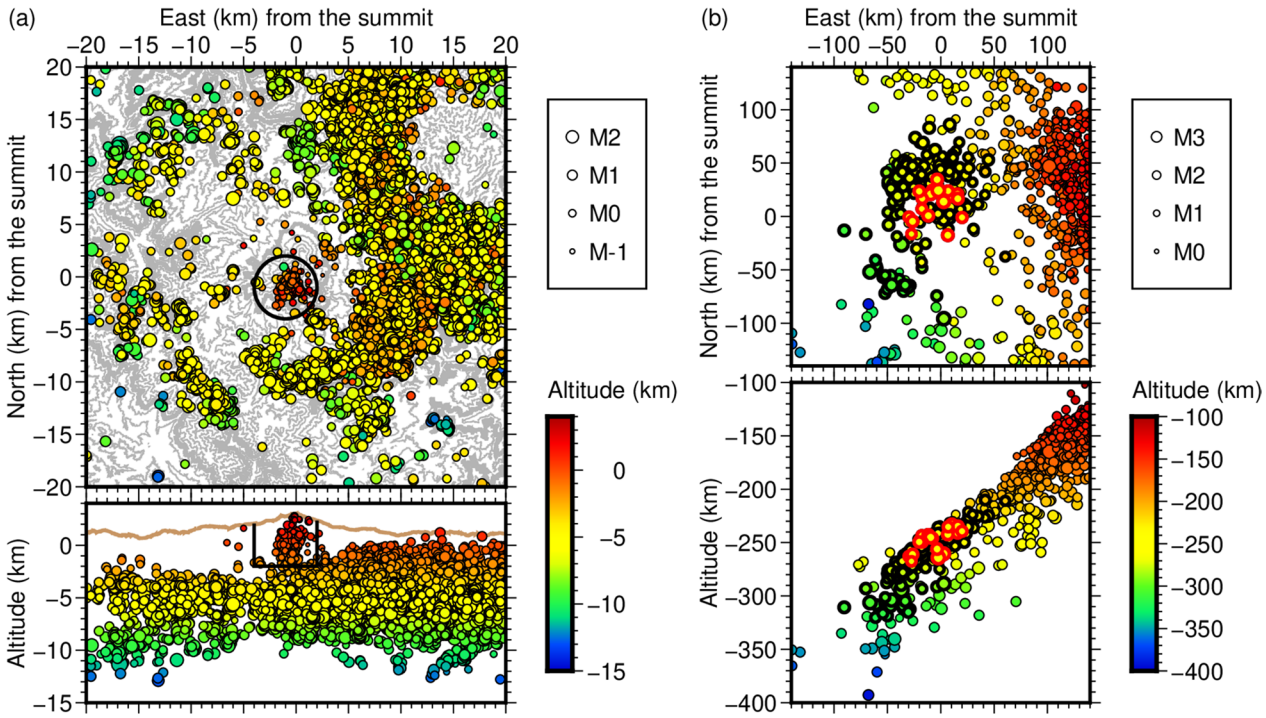

Fig. 2 Hypocentres of the earthquakes around Mt. Ontake during the study period. **a** Local earthquakes located via the routine monitoring of Nagoya University. The black cylinder shows a region of hypocentres regarded as shallow volcanic earthquakes (SVEs). **b** Deep (> 100 km) earthquakes located by the Japan Meteorological Agency. Circles with bold borders show the intermediate-depth earthquakes (IDEs) used in this study. Those with red borders show the IDEs used for the analysis 1

arrival times of $M \geq 0$ SVEs at stations within 10 km from the summit (Fig. 1). Waveforms that showed unclear arrival times because of an emergent onset, a low signal-to-noise (S/N) ratio, or contamination of another earthquake signal were excluded from the analysis to maintain the quality of our picks. The results were 2369 P- and 1723 S-wave arrival times from 89 relatively large and clear SVEs.

We selected $M \geq 2$ IDEs that occurred at $\geq$ 100 km depths from an earthquake catalogue issued by the JMA. We used the IDE waveforms at stations where the incident angles were less than 10° on the basis of the JMA2001 velocity model (Ueno et al. 2002). We manually identified the P-wave arrival time (t_p) of each waveform; it was rejected if the arrival time was difficult to identify or the record was contaminated by another event signal. We also examined the S/N ratio in a high-pass (1 Hz) waveform; both the maximum and root-mean-square (RMS) amplitudes in the signal window (from 2 s before to 18 s after t_p) were required to be more than twice the corresponding quantities in the noise window (22–2 s before t_p). We used the waveforms that satisfied all these requirements (2393 waveforms from 179 IDEs; bold circles in Fig. 2b). Figure 3 shows an example of IDE waveforms with the noise and signal windows.

The use of IDEs was essential to a reliable estimate of the velocity structure. If only the SVEs were used, the reliability of the estimated structure would have been degraded due to the mutual dependence of the SVE altitudes and the velocity structure; the velocity model needed to be assumed to locate the SVEs, and the uncertainty in the model was mapped to the errors in the hypocentres, which in turn affected the estimated velocity model. This loop-back effect was mitigated by the use of the IDEs in addition to the SVEs; the uncertainty in the local structure had almost no effect on the hypocentres of the IDEs. We performed three analyses as described below.

Analysis 1: estimating a typical P-wave velocity in the summit region

Even a typical P-wave velocity was not known in the summit region of Mt. Ontake. We investigated it using the propagation velocity of the IDEs. The P-waves of the IDEs arrived sequentially from lower- to higher-altitude stations because of their almost vertical incidence. We used only the IDE-station pairs that satisfied < 5° incident angles to suppress the deviation from the vertical incidence approximation. We used stations

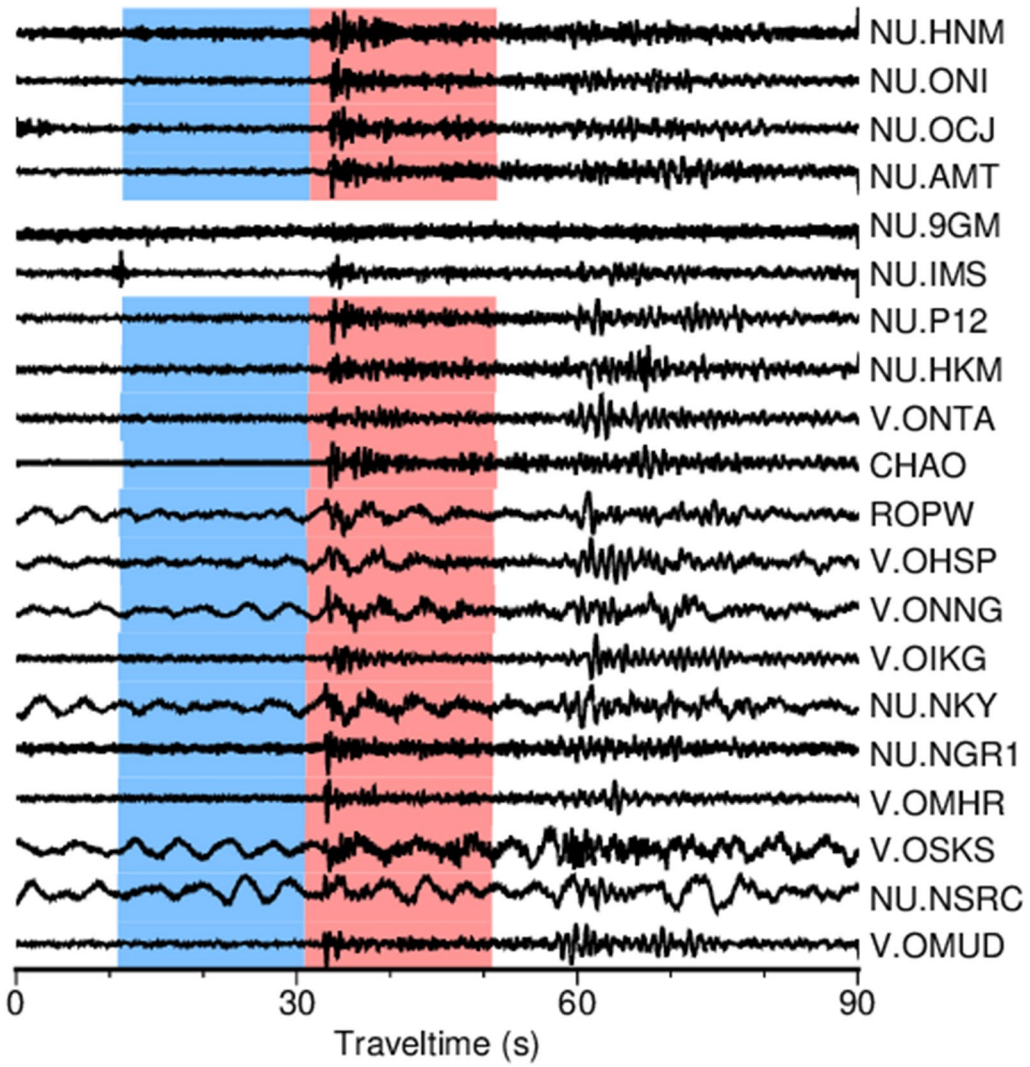

Fig. 3 Example of IDE waveforms. Blue and pink shaded areas are the noise window (22–2 s before t_p) and the signal window (from 2 s before to 18 s after t_p), respectively, where t_p is a manually identified P-wave arrival time. In this example, data from stations NU.9GM and NU.IMS were not used because of a low signal-to-noise ratio or contamination by impulsive noise

located at > 1.5 km asl. (green symbols in Fig. 1), which were close to the summit region. We used only the IDEs that had ≥ 10 waveforms, including ≥ 2 in each altitude range of 1.5–2.0, 2.0–2.5, and > 2.5 km asl. For each IDE, we computed the semblance values (Neidell and Taner 1971), assuming vertical propagation at a constant velocity. We performed grid searches to obtain the maximum semblance, varying the assumed velocity (every 0.1 km/s in 1.0–5.0 km/s) and a time window of 1-s long (every 0.01 s in 25–45 s after the origin time of the IDE). This time window range consisted of expected P-wave arrival times (30–35 s) and did not consist of S-wave arrival times (55–60 s) for the IDEs at ~ 250 km depths.

Analysis 2: estimating a layered P-wave velocity model

We estimated a layered model using the P- and S-wave arrival times of the SVEs. We searched for the optimal model that best explained the arrival times assuming 1–3 horizontal layers, where the deepest layer was a half space. The 3-layer model was expressed by the P-wave velocities in individual layers (V_{p1}–V_{p3} from shallower to deeper) and the shallower (z_{12}) and deeper (z_{23}) boundary altitudes. We assumed the S-wave velocity in each layer to be $1/\sqrt{3}$ times the P-wave velocity.

We performed grid searches for four structural parameters (V_{p2}, V_{p3}, z_{12}, z_{23}) and the hypocentres of individual SVEs. The location that minimized the RMS traveltime residual was considered the hypocentre of each SVE, and the structural parameters that minimized the residuals averaged over all SVEs were considered to be the optimal model. To reduce the number of free parameters, we determined V_{p1} from the other four parameters by letting the average P-wave velocity above 1.5 km asl. from the layered model to be equal to that from the analysis 1. We used grid intervals of 0.1 km for the hypocentres. We sequentially narrowed the search ranges and intervals of the structural parameters as 0.4 km/s and 0.4 km in the first search, 0.2 km/s and 0.2 km in the second search, and 0.1 km/s and 0.1 km in the third search.

Analysis 3: estimating a reflection profile

The autocorrelation function (ACF) of a vertically incident seismic wave at a station provides the reflection response at the station (Claerbout 1968). We computed the ACFs of the vertical waveforms of IDEs that satisfied < 10° incident angles at each station. We used the signal and noise windows (see "Data" section and Fig. 3) to estimate the ACF and its error of each IDE using the method proposed by Maeda and Watanabe (2022). From the ACFs, we computed the reflection responses using the relationship proposed by Claerbout (1968). The reflection responses from all IDEs were then stacked at each station. The stacked reflection response was a function of the lag time. We computed the depth of a reflector corresponding to each lag time, assuming vertical propagation and a single reflection of the P-wave through the velocity structure estimated from the analysis 2. We used a frequency band of 1–10 Hz that was shown to be effective in imaging the depth range of approximately 1–2 km (Maeda and Watanabe 2022), where the shallow hydrothermal system was expected to be present at Mt. Ontake. Throughout this paper, we show the ratio $a^{\mathrm{ave}}(z)/\sigma^{a}(z)$, where $a^{\mathrm{ave}}(z)$ and $\sigma^{a}(z)$ are the ensemble average and standard deviation of the reflection response at each station, respectively; their explicit formulas are provided in Maeda and Watanabe (2022).

Results

Analysis 1: typical P-wave velocity in the summit region

Figure 4a shows the waveform semblance (S) values for each IDE plotted against the assumed P-wave velocity. Although several IDEs showed low S values for all

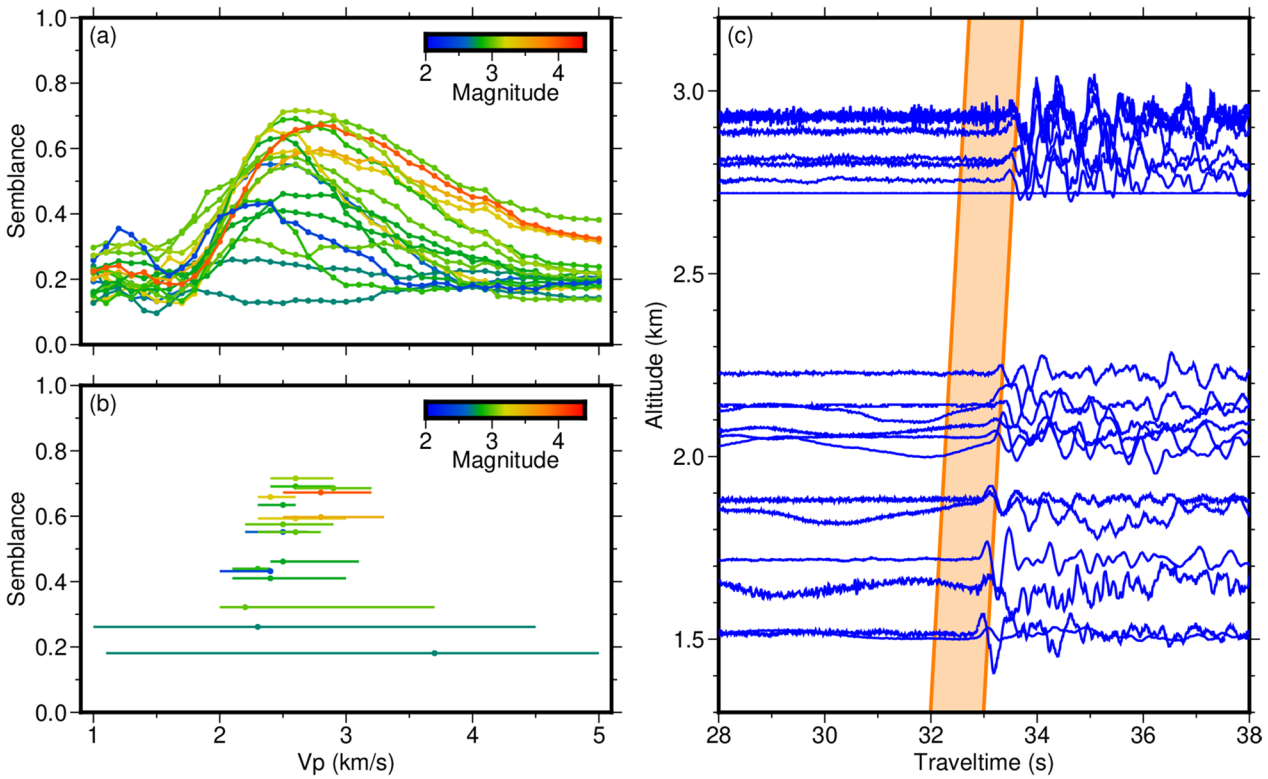

Fig. 4 Results from the analysis 1. **a** Semblance values (S) versus assumed P-wave velocities (V_p) for each intermediate-depth earthquake (IDE). **b** Maximum semblance (S_{max}; the dot) and the range of $S \geq S_{max} - 0.05$ (the bar) for each IDE. **c** Example of IDE waveforms plotted along the station altitudes. The orange time window corresponds to the maximum semblance for this IDE

P-wave velocities, most IDEs showed peaks at 2–3 km/s. This feature was more clearly recognized in Fig. 4b, in which the maximum semblance ($S_{\max}$) and the range of $S \geq S_{\max} - 0.05$ were plotted. Among the 18 analysed IDEs, 15 showed $S_{\max} \geq 0.4$ and relatively narrow velocity ranges for $S \geq S_{\max} - 0.05$. For these events, the P-wave velocity corresponding to $S_{\max}$ was 2.3–2.9 km/s with an average of 2.6 km/s, a median of 2.5 km/s, and a mode of 2.5–2.6 km/s. The number of IDEs that showed $S \geq S_{\max} - 0.05$ was maximal (13 IDEs) for 2.6 km/s. We concluded that 2.6 km/s was the optimal value of the typical P-wave velocity for ≥ 1.5 km asl. beneath Mt. Ontake.

Figure 4c shows the waveforms of a typical IDE plotted versus the station altitudes, indicating a clear vertical propagation of P-wave arrivals. The orange box in this figure shows the time window for the maximum S, indicating that the maximum semblance corresponds to the propagation of the P-wave arrivals.

Analysis 2: layered P-wave velocity model

Table 1 shows the traveltime residuals and Akaike Information Criterion (AIC; Akaike 1974) values obtained assuming 1–3 layers. The AIC values were computed as follows:

$$AIC = 2N\ln E + 2M, \tag{1}$$

where N is the number of data samples, E is the traveltime residual, and M is the number of model parameters. We used $N = 4092$, which was the total number of P- and S-wave arrival times. We used $M = 267$ (89 SVEs × 3 components of locations) for the 1-layer (homogeneous) model; there was no structural parameter in this model because we used the P-wave velocity of 2.6 km/s from the result of the analysis 1. The 3-layer model consisted of four independent structural parameters (V_{p2}, V_{p3}, z_{12}, and z_{23}), resulting in $M = 267 + 4 = 271$. The 2-layer model was the 3-layer model with $V_{p2} = V_{p3}$ and $z_{12} = z_{23}$; two structural parameters were independent in this model, giving $M = 267 + 2 = 269$. For E, we used the RMS traveltime residuals (s) averaged over all SVEs. We did not normalize E; the normalization resulted in a constant shift in the AIC values and did not affect the choice of the optimal model. The traveltime residuals and AIC values (Table 1) indicated that the 3-layer model was optimal.

Table 1 Traveltime residuals and Akaike Information Criterion (AIC; Akaike 1974) values in the analysis 2 assuming 1–3 layers

Model	*E*	*N*	*M*	AIC
1 layer	0.4626 s	4092	267	− 5775
2 layers	0.0804 s	4092	269	− 20092
3 layers (global minimum model)	0.0733 s	4092	271	− 20844
3 layers (final model)	0.0746 s	4092	271	− 20701
NU-summit	0.0931 s	4092	267	− 18895

Figure 5a shows the traveltime residuals of the 2- and 3-layer models plotted in structural parameter space. The minimum traveltime residual of 0.0733 s was obtained for $V_{p2} = 4.3$ km/s, $V_{p3} = 5.6$ km/s, $z_{12} = 1.6$ km, and $z_{23} = 0.8$ km (global minimum model). However, the model was not well constrained, with some trade-off among the structural parameters. For example, increasing z_{12} and decreasing V_{p2} simultaneously from the global minimum model did not significantly increase the traveltime residuals (Fig. 5a). This issue is addressed after obtaining a reflection profile.

Analysis 3: reflection profile

Figure 6a shows the reflection responses from higher to lower altitude stations. They were converted to depth-sections (Fig. 6b) assuming the global minimum velocity model of the analysis 2. The $a^{\mathrm{ave}}(z)/\sigma^{a}(z)$ ratios > +3 and < − 3 were plotted by red and blue colours, respectively; these values corresponded to positive and negative reflectors of > 99% significance level (Maeda and Watanabe 2022).

The ACFs have the largest peak at zero lag time (zero depth), and the following signals in the ACFs could be caused by band-limited incident waves rather than actual reflections in the structure. The shallowest negative peak of ~ 60 m thick and the underlying positive peak of ~ 300–400 m thick in Fig. 6b could be the artefacts caused by this effect, since their presence beneath all stations was unnatural. A similar pair of negative and positive peaks was observed in the metropolitan area of Japan (Maeda and Watanabe 2022). To avoid these potential artefacts in interpretation, we focused on the reflection responses below the second zero-crossing hereafter (green lines in Fig. 6b).

To discover subhorizontal reflectors, we horizontally stacked the reflection responses below the second zero-crossing over all high-altitude (> 2 km) stations. We used weighted stacking, where the inverse of the variance was used as the weight. The result (Fig. 6c) showed clear positive peaks at 1.8 km asl., 0.9 km asl., and 0.4 km below sea level (bsl.). The altitudes of the upper two peaks were close to those of the velocity discontinuities estimated in the analysis 2 (Fig. 6d), suggesting that the two analyses pointed to the same material boundary.

Combined analysis

Figure 5a shows that the structural model was not well constrained by the traveltime residuals alone. We aimed to better constrain it by combining the reflection responses. As the reflection occurs at the velocity

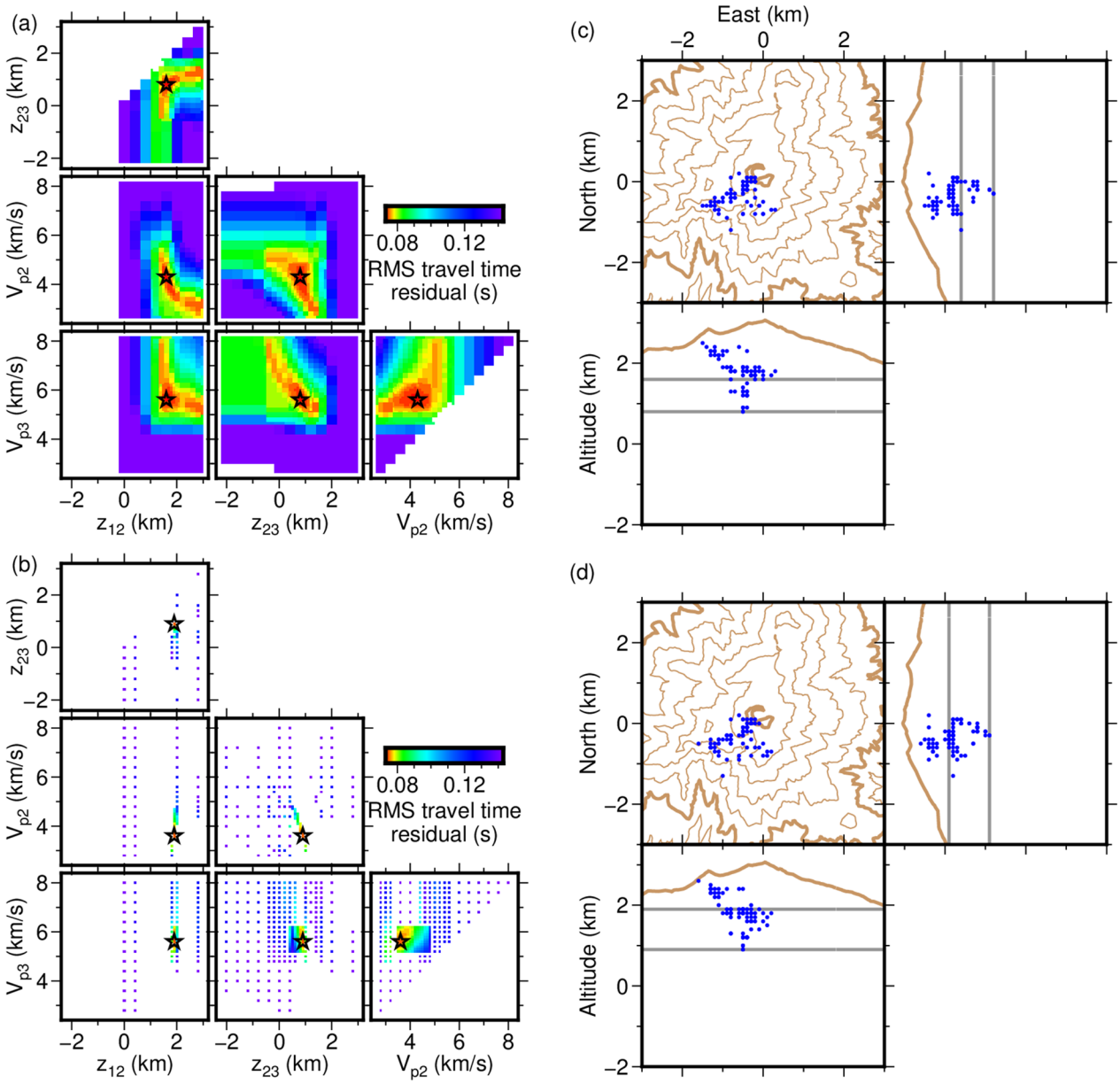

Fig. 5 Results from the analysis 2. **a** Root mean square (RMS) traveltime residuals for the four structural parameters searched. Stars indicate the solution that minimized the residual. **b** Same as Fig. 5a but for limited combinations of the four parameters that satisfied less than ± 0.05 km differences between the layer boundary altitudes from the analysis 2 and the reflector altitudes from the analysis 3. **c** Hypocentres of the shallow volcanic earthquakes (SVEs) used for the analysis 2 from the global minimum model (**a**) and **d** final model (**b**). Horizontal bars show the layer boundaries

discontinuities, the modelled layer boundaries in the analysis 2 were expected to be consistent with reflector altitudes in the analysis 3. This assumption was supported by Fig. 6c, which showed prominent reflectors at altitudes close to z_{12} and z_{23} (Fig. 6d). However, there were some differences between the reflector and discontinuity altitudes. We attributed this difference to an inaccurate velocity model due to the poor constraints in the analysis 2 (Fig. 5a). We searched for an alternative model that could provide a better match between the discontinuity and reflector altitudes.

Figure 5b shows the traveltime residuals for limited combinations of the values of the four parameters that satisfied less than ± 0.05 km differences between the discontinuity and reflector altitudes; since we used 0.1 km for the search intervals of z_{12} and z_{23}, the

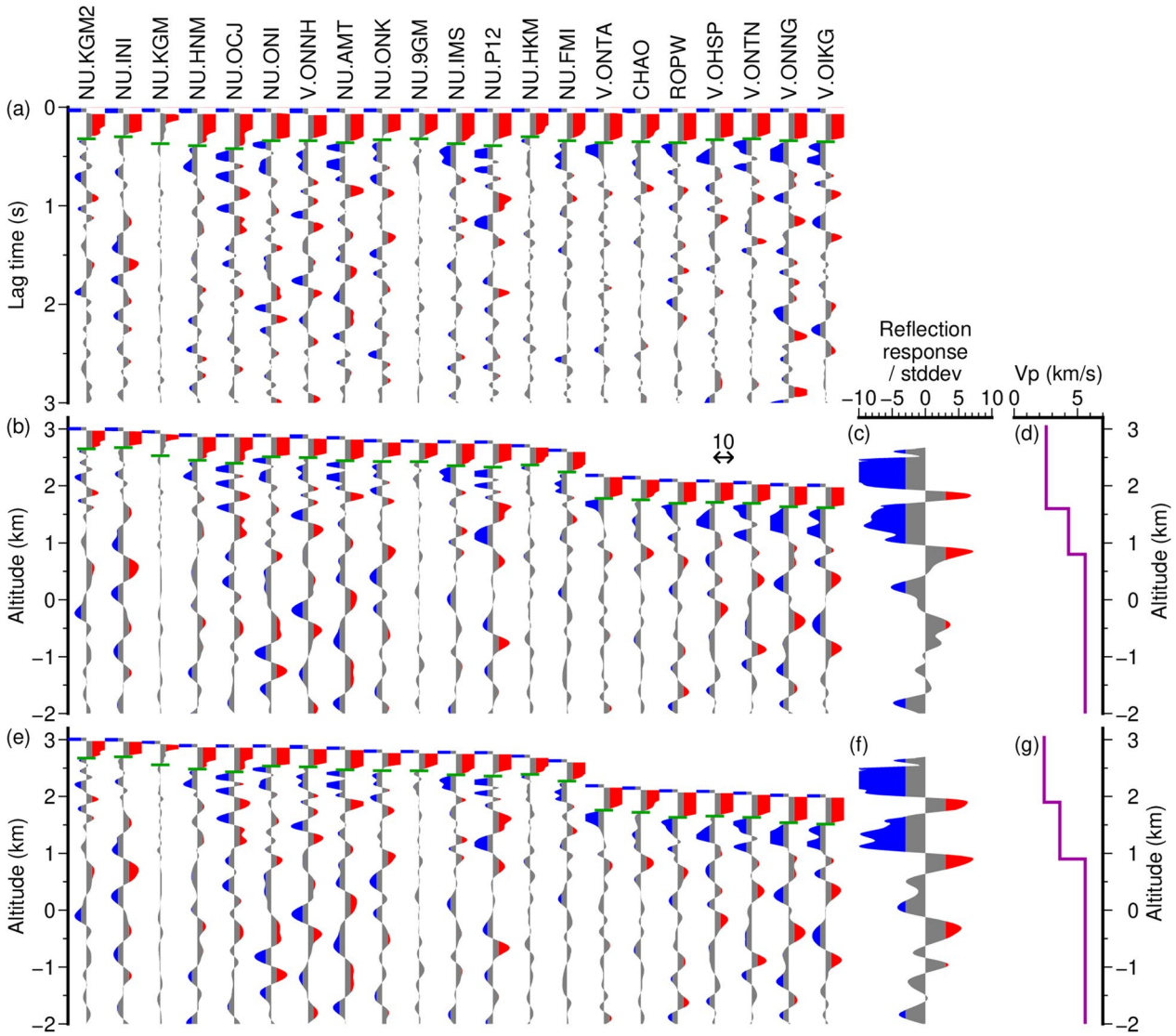

Fig. 6 Results from the analysis 3. **a** Reflection responses at individual stations from higher to lower altitudes. The station codes are shown at the top. The responses are normalized via the standard deviation at each lag time (Maeda and Watanabe 2022). Red and blue colours show the normalized responses of > 3 and < -3, respectively. Green bars show the second zero-crossing. **b** Depth section of the responses calculated from Fig. 6a assuming the global minimum velocity model of the analysis 2. **c** Reflection responses stacked for the same altitudes. **d** P-wave velocities (global minimum model) used for the conversion from the time-section to depth-section in **b**. **e**–**g** Same as **b**–**d** except that the final velocity model of the analysis 2 was used

differences of less than $\pm$ 0.05 km meant the best possible consistency between the altitudes. Among the velocity models that satisfied this requirement, the traveltime residual was minimal for $V_{p2} = 3.6$ km/s, $V_{p3} = 5.6$ km/s, $z_{12} = 1.9$ km, and $z_{23} = 0.9$ km (final model). This model increased the traveltime residual from the global minimum model by only 0.0013 s (Table 1), which was one-seventh the sampling interval of the seismic records, indicating that both models nearly equally explained the traveltimes.

Figure 5c and d shows the hypocentres from the global minimum and final models, respectively. They were located on search grids with 100 m intervals. The hypocentres from the two models showed similar patterns, composed of subvertical (slightly southwest-dipping) and subhorizontal hypocentre distributions below and around 1.9 km asl., respectively, and a shallower cluster to the southwest. The subhorizontal part of the hypocentres was shallower than z_{12} in the global minimum model and close to z_{12} in the final model.

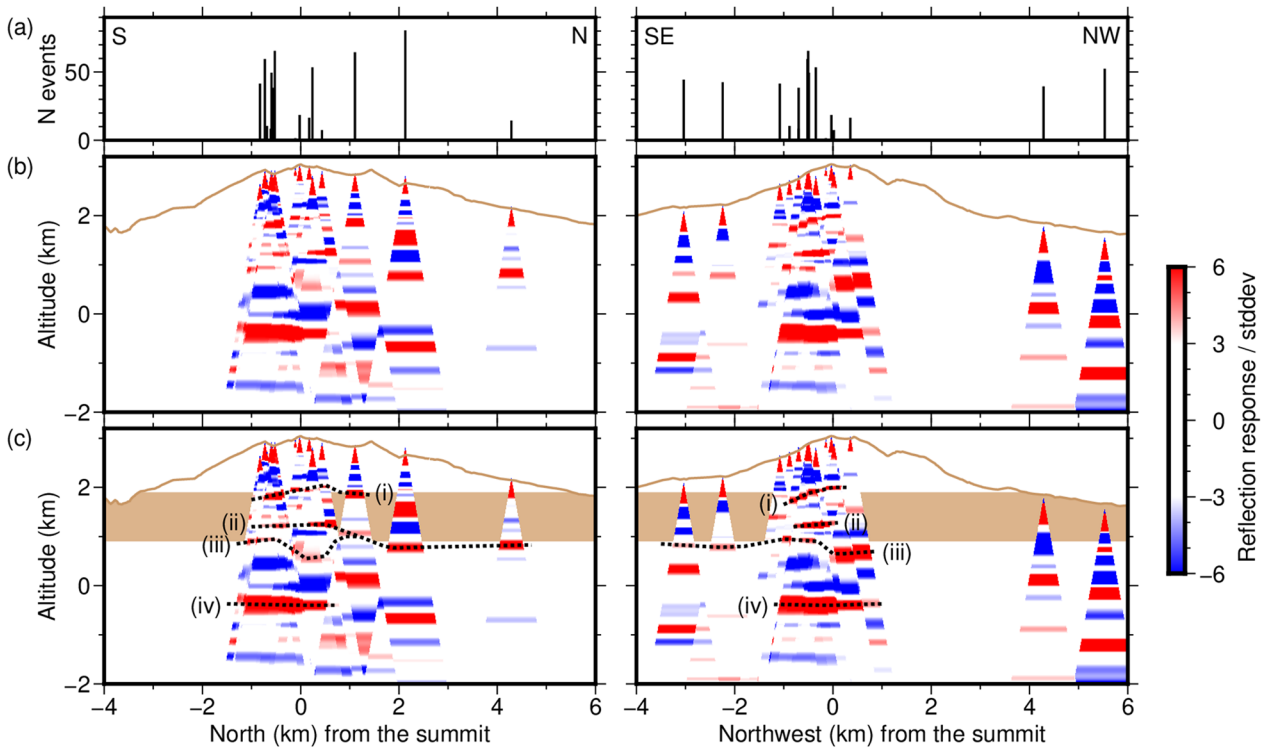

Fig. 7 Results from the analysis 3. The north–south and northwest–southeast transects (purple and orange colours in Fig. 1) are shown. The maximum incident angle of the intermediate-depth earthquakes (10°) was considered in this plot. **a** Number of events stacked for each station. **b** Reflection responses obtained via the final velocity model of the analysis 2. **c** Same as **b** with interpretation. The background brown colour shows layer 2 from the analysis 2

Figure 6e and f shows the reflection responses obtained by the final model. Three reflectors were prominent at 1.9 km asl., 0.9 km asl., and 0.3 km bsl., and the upper two were consistent with z_{12} and z_{23} (Fig. 6g). Figure 7 shows the reflection responses along the N–S and northwest–southeast (NW–SE) transects (Fig. 1a). Four horizontally continuous positive reflectors (i–iv) were prominent. The altitudes of reflectors (i), (iii), and (iv) were close to those of the three positive peaks in Fig. 6f. Reflector (ii) could potentially be a branch of reflector (iii) or an independent local reflector. Reflector (iv) was localized beneath the summit region.

Discussion

Reliability and importance of the estimated structure

Although this study was the first seismic structural survey in the summit region of Mt. Ontake, there were several surveys in the surrounding region. Ikami et al. (1986) conducted a ~ 200 km length refraction experiment with artificial explosion sources. One end of the survey line was ~ 10 km southeast from the summit of Mt. Ontake. In this region, they found three layers with P-wave velocities of 2.8, 3.9, and 5.9 km/s. These values are close to the results of our study (2.4, 3.6, and 5.6 km/s). Doi et al. (2013) performed tomography in the southeastern region of Mt. Ontake using the LTEs. Although their result was a continuous rather than a layered velocity model for a relatively deep ($\lesssim$ 1 km asl.) part, their estimated P-wave velocity of ~ 5 km/s at 1 km asl. did not conflict with the velocity estimated in our study, which increased from 3.6 to 5.6 km/s near this altitude. The velocity of ~ 5.6 km/s at ~ 1–3 km bsl. from Doi et al. (2013) was also consistent with the results of our study.

The analyses 2 and 3 comprised largely independent investigations of subsurface boundaries. Although the velocity model from the analysis 2 was used to convert from the time-section to depth-sections of the reflection responses in the analysis 3, this had only subtle effects on the estimated reflection profiles (Fig. 6c and f). The reflectors from the analysis 3 were imaged near the altitudes of velocity discontinuities from the analysis 2, even in the case of separate analyses (Fig. 6c and d). Therefore, the results from the two analyses are mutually supported.

The subsurface structure has significant effects on the determination of the hypocentres of SVEs. The blue line in Fig. 8a is the velocity model used for routine seismicity monitoring by Nagoya University (the NU-routine model). The red line is the final velocity model of this

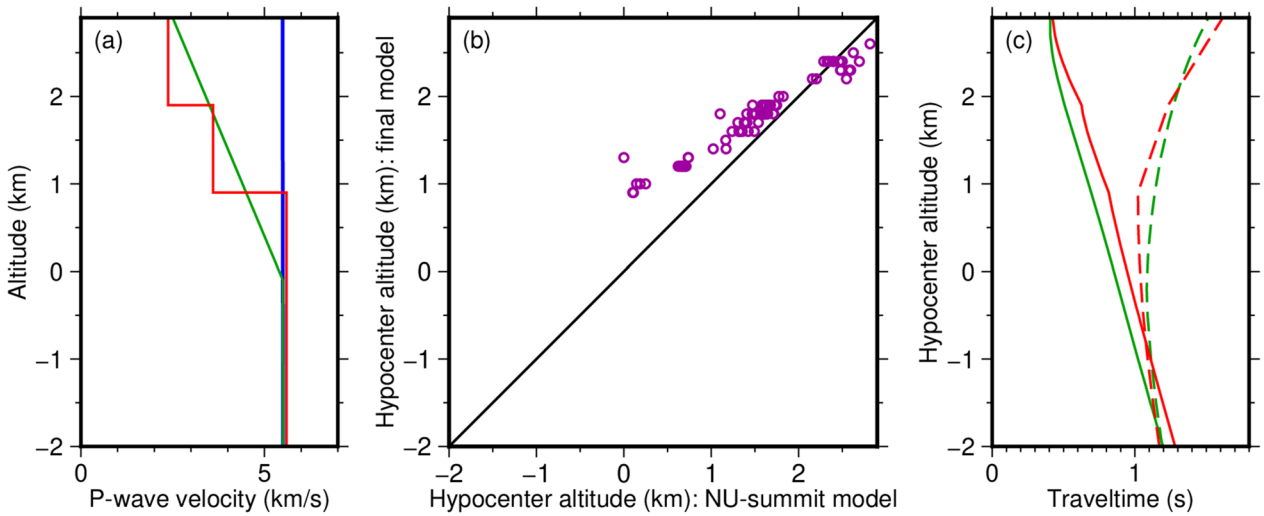

Fig. 8 Effects of assumed velocity structures on hypocentre locations. **a** Three velocity models considered (blue: the NU-routine model, green: the NU-summit model, red: the final model). **b** Comparison of the hypocentre altitudes of shallow volcanic earthquakes (SVEs) used for the analysis 2. The lateral and vertical axes are the altitudes obtained via the NU-summit and final models, respectively. **c** Theoretical traveltimes from various hypocentre altitudes assuming the NU-summit (green) and final (red) models. Solid and dashed lines are the traveltimes at typical summit (epicentral distance: 1 km, altitude: 3 km asl.) and flank (epicentral distance: 5 km, altitude: 1.5 km asl.) stations, respectively

study, and the green line is an approximated model (the NU-summit model) to accommodate the monitoring system which requires that the velocities vary linearly with the altitudes above sea level. Because a direct comparison of the NU-routine and final models was not available, we first compared the NU-routine and NU-summit models. Approximately one-third of the SVEs were located above the ground surface with the NU-routine model when the data from the summit trial stations were included. Most of these SVEs were located below the ground surface with the NU-summit model, showing its superior performance compared to the NU-routine model. We concluded that the NU-summit model was better than the NU-routine model in terms of stable estimation of hypocenters. We now move to a comparison of the NU-summit and final models. From Fig. 8b, the altitudes of relatively deep SVEs from the NU-summit model were underestimated compared to those from the final model. This was probably because the NU-summit model underestimated and overestimated the traveltimes at summit and flank stations, respectively (Fig. 8c). As a result, an observed traveltime difference between summit and flank stations was explained by a deeper source in the NU-summit than in the final model, causing the hypocentre depth difference (Fig. 8b). A comparison of the traveltime residuals from the two models (Table 1) showed that the final model was better. In conclusion, the approximation of the final model by the NU-summit model introduced some errors in the hypocentre altitudes, especially for relatively deep SVEs.

Interpretation

Figure 9 compiles the final velocity model (Fig. 9b), hypocentres of the SVEs from the analysis 2 (Fig. 9a, green), and the reflection profile from the analysis 3. Also shown are the hypocentres of all SVEs during the study period (Fig. 9a, grey); we relocated them using the P- and S-wave arrival times picked via the routine seismicity monitoring of Nagoya University but with the final velocity model. We used a grid search of 20 m intervals to relocate them.

The analyses 2 and 3 indicated layer boundaries at ~ 1.9 and 0.9 km asl. The altitude of 1.9 km was close to the surface distribution of the Y–O boundary except for several leaves of flow-like parts to downwards (Fig. 1a), suggesting that the first and second layers were the YED and OED, respectively (Fig. 9a). Due to the long (~ 0.3 Ma) dormant period after the older activity, the OED was expected to be more compacted and cemented than the YED, causing a velocity discontinuity. A resultant water saturation differences could also have affected the velocity differences between the two layers. The flowing parts of the YED could be too thin to be imaged seismically. Asai et al. (2006) showed a large amount of water discharge along the Y–O boundary and proposed a groundwater flow along the boundary. From Fig. 1a, most rivers around Mt. Ontake originated from ~ 1.9 km asl. These observations were consistent with the hypothesis of a relatively low permeability in the OED beneath ~ 1.9 km asl. due to physical compaction or chemical cementation.

We interpreted the third layer as the basement (Fig. 9a) because the top of the basement was the most likely

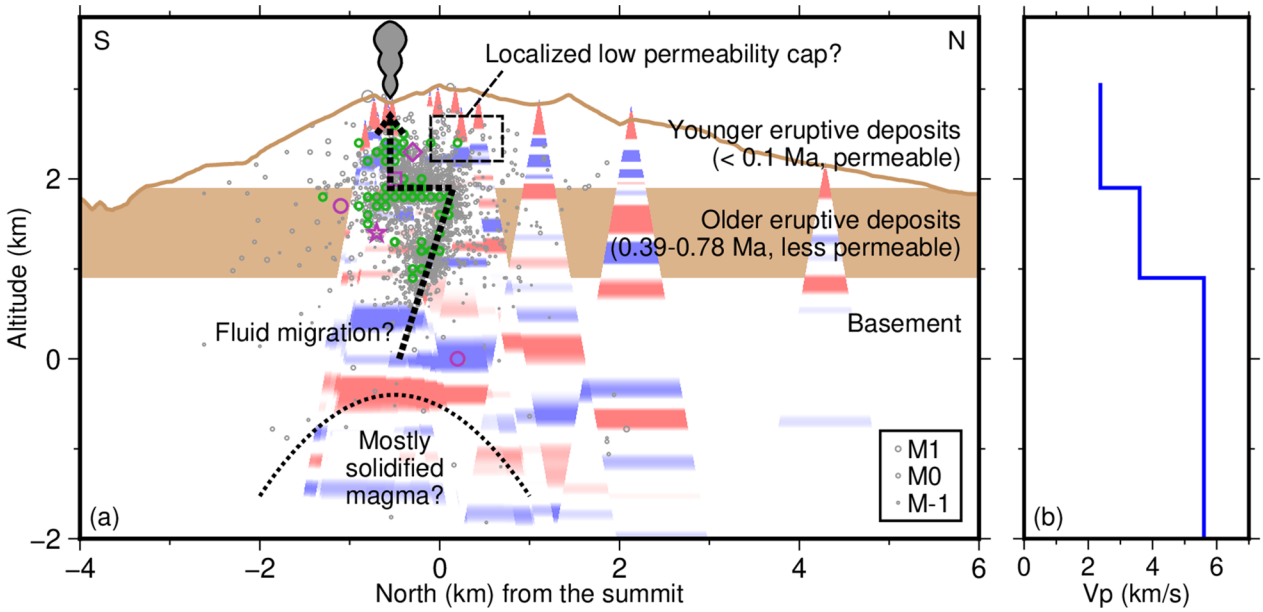

Fig. 9 Summary and interpretation of this study on the north–south transect. The reflection responses from the analysis 3 (Fig. 7b) and the final velocity model from the analysis 2 are plotted with hypocentres and crustal deformation sources. Green circles are the hypocentres of shallow volcanic earthquakes (SVEs) from the analysis 2. Grey circles are the hypocentres of all SVEs during the study period relocated using the final model and the P- and S-wave arrival times picked by the routine analysis of Nagoya University. The circle size scales with the magnitude shown at the bottom right. The purple circles, star, square, and diamond are the sources of inflation two months before the 2007 eruption (Takagi and Onizawa 2016), a tilt change that started 450 s before the 2014 eruption (Maeda et al. 2017), a very long period seismic event 25 s before the 2014 eruption (Maeda et al. 2015b), and a deflation that has continued over several years after the 2014 eruption (Narita and Murakami 2018), respectively. The broken arrow indicates a possible pathway of the fluid migration suggested by the hypocentre distribution

discontinuity that was expected to be present beneath the OED. The P-wave velocity of 5.6 km/s in the third layer was close to the value of 5.9 km/s from Ikami et al. (1986), who interpreted the third layer as the basement. Figure 7 suggests that this boundary had a complicated geometry.

The purple star in Fig. 9a is the modelled source location of a tilt change that started 450 s before the 2014 eruption. Maeda et al. (2017) interpreted this tilt change as having been caused by the upward migration of water vapour creating a new pathway by breaking intact rock that had acted as a permeability barrier at this depth. The horizontal location of the tilt source was not constrained within the search range of 0.8×0.8 km, whereas the depth was relatively well constrained (Maeda et al. 2017). The source was in the OED layer (Fig. 9a), suggesting that the OED acted as a barrier for fluid migration at the time of the 2014 eruption.

The hypocentres were elongated horizontally along the Y–O boundary and subvertically through the OED layer (Fig. 9a). We considered these features as an indicator of subsurface fluid flow because an increased pore fluid pressure decreases the effective strength of the host rock, which could cause earthquakes. We speculated two potential sources of fluids. One was abundant underground water along the Y–O boundary, as suggested by the subhorizontal distribution of the hypocenters along the boundary and the model of Asai et al. (2006). The other was volcanic fluid from a greater depth, as suggested by the subvertical distribution of the hypocenters through the OED layer. Seismicity in the YED layer occurred in the southwestern side from the summit, where the 2014 eruptive craters (Fig. 1b), the source of a very long period event 25 s before the 2014 eruption (the purple square in Fig. 9a; Maeda et al. 2015b) and the source of deflation after 2014 (the purple diamond in Fig. 9a; Narita and Murakami 2018) were present. The entire hypocentre distribution in Fig. 9a suggested that the volcanic fluid migrated upwards through the OED, stopped ascending at the Y–O boundary, and moved horizontally southwestward until it reached below the currently active site. The lateral movement of the fluid implied a localized low-permeability cap in the YED layer immediately above the bending point of the seismicity (Fig. 9a). Although we have no structural evidence for this cap, the presence of crater lakes from the summit to the north of Mt. Ontake (Fig. 1b) implied that the shallow part in this region was not highly permeable. In this region, the solidification of past activity deposits may have been conductive to the development of the

low-permeability cap. A similar scenario was proposed for Asama volcano, Japan (Aizawa et al. 2008).

Another localized reflector was imaged at ~ 0.3 km bsl. (Fig. 6f) beneath the summit region (Fig. 7). A possible explanation for this reflector may be the roof of a magma reservoir. A high-temperature molten magma was unlikely since the positive polarity of the reflector indicated a higher velocity beneath it than above. Tomographic studies at several volcanoes consistently showed a high-velocity anomaly at a few kilometre depths interpreted as an old, solidified magma (e.g. Tanaka et al. 2002; Yamawaki et al. 2004; Aoki et al. 2009). The roof depths and horizontal dimensions of these anomalies were similar to those of the localized reflector obtained in our study (Fig. 7), suggesting that the scenario of an old, solidified magma may be a clue to interpret the reflector. However, the hypocentre distribution suggested fluid migration from near this reflector, implying some fluid-related activity in this region (Fig. 9a). There was almost no seismicity beneath this reflector. We speculated that the region beneath this reflector was a mostly solidified crystal mush at a temperature slightly above the brittle–ductile transition. The cooling and resultant crystallization of the mush was still ongoing, which may have caused the exsolution of volatiles (e.g. Edmonds and Woods 2018). Despite a slightly higher temperature than the surroundings, an absence of fractures could result in a high-velocity anomaly (Scheu et al. 2006). The crustal deformation source near the roof of this potential reservoir (the lower purple circle in Fig. 9a; Takagi and Onizawa 2016) supported this interpretation. The deformation likely occurs not at the centre but near the roof of a magma reservoir (e.g. Edmonds and Woods 2018; Tameguri et al. 2022). Narita et al. (2019) proposed a deep source of the deflation after the 2014 eruption at 0–3 km bsl., consistent with the cooling magma reservoir in Fig. 9a.

The discussion above is based on the 1-D velocity model, a reflection image, and the spatial distributions of hypocentres and crustal deformation sources. Direct investigations of the P- and S-wave velocities are the next research step to examine the hypothesis of the localized low-permeability cap in the YED and the mostly solidified magma.

Conclusions

We investigated a shallow subsurface structure in the summit region of Mt. Ontake, central Japan, from three seismic analyses. First, we estimated a typical P-wave velocity for > 1.5 km asl. from the semblance analysis of the vertical propagation velocity of the IDEs. Second, we estimated a layered structure from the P- and S-wave arrival times of SVEs. Third, we performed pseudoreflection imaging from the ACFs of the IDE waveforms. The results consistently showed three layers with boundaries at 1.9 and 0.9 km asl. They were interpreted as the YED, OED, and the basement. The OED potentially had relatively low permeability due to long-term compaction and cementation and acted as a permeability barrier. The hypocentre distribution suggested a subvertical fluid flow through the OED and a subhorizontal flow along the Y–O boundary towards the currently active craters.

Acknowledgements

We used seismic waveform records from Nagoya University, the Japan Meteorological Agency (JMA), and the Nagano and Gifu Prefectures. The monitoring network at Nagoya University has been maintained by Yoshiko Yamanaka, Toshiko Terakawa, and Shinichiro Horikawa. We used a unified earthquake catalogue issued by the JMA. We used map data from the Geospatial Infomation Authority of Japan. In Fig. 9, we used the P- and S-wave arrival times of SVEs picked by Junko Sumida and Eri Hibino at Nagoya University. Comments by two anonymous reviewers helped to improve the manuscript. This work was supported by JSPS KAKENHI Grant Number JP19K04016. This work was also supported by the Ministry of Education, Culture, Sports, Science and Technology (MEXT) of Japan, under its The Second Earthquake and Volcano Hazards Observation and Research Program (Earthquake and Volcano Hazard Reduction Research).

Author contributions

YM conducted the data analyses and drafted the manuscript. TW provided several important suggestions and edited the manuscript.

Funding

JSPS KAKENHI Grant Number JP19K04016. The Ministry of Education, Culture, Sports, Science and Technology (MEXT) of Japan, under its The Second Earthquake and Volcano Hazards Observation and Research Program (Earthquake and Volcano Hazard Reduction Research).

Availability of data and materials

Raw data obtained by Nagoya University and derived data are available upon request to the corresponding author. Most computer codes used in the analysis are available from ymaeda_opentools (Maeda 2022).

Declarations

Competing interests

The authors declare that they have no competing interests.

Author details

[1]Graduate School of Environmental Studies, Nagoya University, D2-2 (510) Furo-cho, Chikusa-ku, Nagoya, Aichi 464-8601, Japan.

Received: 11 May 2023 Accepted: 7 July 2023
Published online: 19 July 2023

References

Abd Allah S, Mogi T (2016) Three-dimensional resistivity modeling of GREATEM survey data from Ontake Volcano, northwest Japan. Earth Planets Space 68:76. https://doi.org/10.1186/s40623-016-0443-z

Aizawa K, Ogawa Y, Hashimoto T, Koyama T, Kanda W, Yamaya Y, Mishina M, Kagiyama T (2008) Shallow resistivity structure of Asama Volcano and its implications for magma ascent process in the 2004 eruption. J Volcanol Geotherm Res 173(3–4):165–177. https://doi.org/10.1016/j.jvolgeores.2008.01.016

Akaike H (1974) A new look at the statistical model identification. IEEE Trans Autom Control 19(6):716–723. https://doi.org/10.1109/TAC.1974.1100705

Aoki Y, Takeo M, Aoyama H, Fujimatsu J, Matsumoto S, Miyamachi H, Nakamichi H, Ohkura T, Ohminato T, Oikawa J, Tanada R, Tsutsui T, Yamamoto K, Yamamoto M, Yamasato H, Yamawaki T (2009) P-wave velocity structure beneath Asama Volcano Japan, inferred from active source seismic experiment. J Volcanol Geotherm Res 187(3–4):272–277. https://doi.org/10.1016/j.jvolgeores.2009.09.004

Asai K, Satake H, Tsujimura M (2006) Characteristics of groundwater flow in Ontake stratovolcano, central Japan, with reference to erosion conditions. J Groundwater Hydrol 48(4):279–296. https://doi.org/10.5917/jagh1987.48.279

Christenson BW, Reyes AG, Young R, Moebis A, Sherburn S, Cole-Baker J, Britten K (2010) Cyclic processes and factors leading to phreatic eruption events: Insights from the 25 September 2007 eruption through Ruapehu Crater Lake, New Zealand. J Volcanol Geotherm Res 191(1–2):15–32. https://doi.org/10.1016/j.jvolgeores.2010.01.008

Claerbout JF (1968) Synthesis of a layered medium from its acoustic transmission response. Geophysics 33(2):264–269. https://doi.org/10.1190/1.1439927

Dempsey DE, Cronin SJ, Mei S, Kempa-Liehr AW (2020) Automatic precursor recognition and real-time forecasting of sudden explosive volcanic eruptions at Whakaari, New Zealand. Nat Commun 11:3562. https://doi.org/10.1038/s41467-020-17375-2

Doi I, Noda S, Iio Y, Horiuchi S, Sekiguchi S (2013) Relationship between hypocentral distributions and Vp/Vs ratio structures inferred from dense seismic array data: a case study of the 1984 western Nagano Prefecture earthquake, central Japan. Geophys J Int 195(2):1323–1336. https://doi.org/10.1093/gji/ggt312

Edmonds M, Woods AW (2018) Exsolved volatiles in magma reservoirs. J Volcanol Geotherm Res 368:13–30. https://doi.org/10.1016/j.jvolgeores.2018.10.018

Gaete A, Walter TR, Bredemeyer S, Zimmer M, Kujawa C, Marin LF, Martin JS, Parra CB (2020) Processes culminating in the 2015 phreatic explosion at Lascar volcano, Chile, evidenced by multiparametric data. Nat Hazards Earth Syst Sci 20(2):377–397. https://doi.org/10.5194/nhess-20-377-2020

Hirahara K, Ikami A, Ishida M, Mikumo T (1989) Three-dimensional P-wave velocity structure beneath Central Japan: low-velocity bodies in the wedge portion of the upper mantle above high-velocity subducting plates. Tectonophysics 163(1–2):63–73. https://doi.org/10.1016/0040-1951(89)90118-2

Hirahara K, Hirata N, Ikami A, Miyamachi H, Yabuki T, Aoki H, Fujii I, Haneda T, Hasegawa A, Hashimoto S, Hirano N, Horiuchi S, Iio Y, Ishiketa Y, Ito A, Ito K, Kanazawa T, Kaneshima S, Karakama I, Kobayashi M, Koizumi M, Kono T, Kosuga M, Kurata Y, Kuriyama S, Kuroiso A, Matsuzawa T, Mikumo T, Mitsunami T, Miura K, Miura K, Miyajima R, Mizoue M, Moriya T, Nakajima A, Nakamura I, Nakamura M, Nakamura T, Nishigami K, Oike K, Okamoto T, Okura T, Ooida T, Ouchi T, Saeki T, Sakai K, Shibutani T, Suzuki M, Suzuki S, Takahashi M, Takagi A, Takeuchi F, Tanada T, Tomita S, Tsukuda T, Umeda Y, Wada H, Yamada M, Yamamoto A, Yamashina K, Yamazaki F, Yokohama M (1992) Three-dimensional P and S wave velocity structure in the focal region of the 1984 Western Nagano Prefecture Earthquake. J Phys Earth 40(2):343–360. https://doi.org/10.4294/jpe1952.40.343

Hirata N, Matsu'ura M (1987) Maximum-likelihood estimation of hypocentre with origin time eliminated using nonlinear inversion technique. Phys Earth Planet Inter 47:50–61. https://doi.org/10.1016/0031-9201(87)90066-5

Hirose F, Nakajima J, Hasegawa A (2008) Three-dimensional seismic velocity structure and configuration of the Philippine Sea slab in southwestern Japan estimated by double-difference tomography. J Geophys Res 113:B09315. https://doi.org/10.1029/2007JB005274

Horikawa S, Okuda T, Maeda Y, Terakawa T, Yamanaka Y, Ogiwara H, Kashiwabuchi K, Yamaguchi M, Igarashi T, Kimura T (2017) Development of portable seismic observation and telemetry equipment. Abst Volcanol Soc Jpn. P036. 2017.

Ichihara H, Kanehiro J, Mogi T, Yamaoka K, Tada N, Bertrand EA, Adachi M (2018) A 3D electrical resistivity model around the focal zone of the 2017 southern Nagano Prefecture earthquake (MJMA 5.6): implications for relationship between seismicity and crustal heterogeneity. Earth Planets Space 70:182. https://doi.org/10.1186/s40623-018-0950-1

Ikami A, Yoshii T, Kubota S, Sasaki Y, Hasemi A, Moriya T, Miyamachi H, Matsu'ura RS, Wada K (1986) A seismic-refraction profile in and around Nagano Prefecture, central Japan. J Phys Earth 34(6):457–474. https://doi.org/10.4294/jpe1952.34.457

Ikami A, Asano S, Koketsu K, Moriya T, Ito K, Tanada T, Yoshida K, Yabuki T, Hirata N (1992) A shallow crustal structure as derived from an explosion seismic experiment. J Phys Earth 40(2):361–377. https://doi.org/10.4294/jpe1952.40.361

Ikehata K, Maruoka T (2016) Sulfur isotopic characteristics of volcanic products from the September 2014 Mount Ontake eruption, Japan. Earth Planets Space 68:116. https://doi.org/10.1186/s40623-016-0496-z

Inamori T, Horiuchi S, Hasegawa A (1992) Location of mid-crustal reflectors by a reflection method using aftershock waveform data in the focal area of the 1984 Western Nagano Prefecture Earthquake. J Phys Earth 40(2):379–393. https://doi.org/10.4294/jpe1952.40.379

Jolly AD, Jousset P, Lyons JJ, Carniel R, Fournier N, Fry B, Miller C (2014) Seismo-acoustic evidence for an avalanche driven phreatic eruption through a beheaded hydrothermal system: an example from the 2012 Tongariro eruption. J Volcanol Geotherm Res 286:331–347. https://doi.org/10.1016/j.jvolgeores.2014.04.007

Kaneko T, Maeno F, Nakada S (2016) 2014 Mount Ontake eruption: characteristics of the phreatic eruption as inferred from aerial observations. Earth Planets Space 68:72. https://doi.org/10.1186/s40623-016-0452-y

Kato A, Terakawa T, Yamanaka Y, Maeda Y, Horikawa S, Matsuhiro K, Okuda T (2015) Preparatory and precursory processes leading up to the 2014 phreatic eruption of Mount Ontake, Japan. Earth Planets Space 67:111. https://doi.org/10.1186/s40623-015-0288-x

Kosuga M (1992) Dependence of coda Q on frequency and lapse time in the western Nagano region, central Japan. J Phys Earth 40(2):421–445. https://doi.org/10.4294/jpe1952.40.421

Maeda Y (2022) ymaeda_opentools. Zenodo. https://doi.org/10.5281/zenodo.6976106

Maeda Y, Watanabe T (2022) Estimating errors in autocorrelation functions for reliable investigations of reflection profiles. Earth Planets Space 74:48. https://doi.org/10.1186/s40623-022-01606-5

Maeda Y, Kumagai H, Lacson R, Figueroa MS, Yamashina T, Ohkura T, Baloloy AV (2015a) A phreatic explosion model inferred from a very long period seismic event at Mayon Volcano, Philippines. J Geophys Res Solid Earth 120(1):226–242. https://doi.org/10.1002/2014JB011440

Maeda Y, Kato A, Terakawa T, Yamanaka Y, Horikawa S, Matsuhiro K, Okuda T (2015b) Source mechanism of a VLP event immediately before the 2014 eruption of Mt. Ontake, Japan. Earth Planets Space 67:187. https://doi.org/10.1186/s40623-015-0358-0

Maeda Y, Kato A, Yamanaka Y (2017) Modeling the dynamics of a phreatic eruption based on a tilt observation: barrier breakage leading to the 2014 eruption of Mount Ontake, Japan. J Geophys Res Solid Earth 122(2):1007–1024. https://doi.org/10.1002/2016JB013739

Maeno F, Nakada S, Oikawa T, Yoshimoto M, Komori J, Ishizuka Y, Takeshita Y, Shimano T, Kaneko T, Nagai M (2016) Reconstruction of a phreatic eruption on 27 September 2014 at Ontake volcano, central Japan, based on proximal pyroclastic density current and fallout deposits. Earth Planets Space 68:82. https://doi.org/10.1186/s40623-016-0449-6

Mannen K, Roman D, Leonard G, Prejean S, Nakagawa M (2019) Special issue "Towards forecasting phreatic eruptions: examples from Hakone volcano and some global equivalents." Earth Planets Space 71:91. https://doi.org/10.1186/s40623-019-1068-9

Métaxian J-P, Santoso AB, Caudron C, Cholik N, Labonne C, Poiata N, Beauducel F, Monteiller V, Fahmi AA, Rizal MH, Nandaka IGMA (2020) Migration of seismic activity associated with phreatic eruption at Merapi volcano, Indonesia. J Volcanol Geotherm Res 396:106795. https://doi.org/10.1016/j.jvolgeores.2020.106795

Miller CA, Kang SG, Fournier D, Hill G (2018) Distribution of and condensate in a hydrothermal system: insights from self-potential inversion at Mount Tongariro, New Zealand. Geophys Res Lett 45(16):8190–8198. https://doi.org/10.1029/2018GL078780

Miyagi I, Geshi N, Hamasaki S, Oikawa T, Tomiya A (2020) Heat source of the 2014 phreatic eruption of Mount Ontake, Japan. Bull Volcanol 82:33. https://doi.org/10.1007/s00445-020-1358-x

Miyaoka K, Takagi A (2016) Detection of crustal deformation prior to the 2014 Mt. Ontake eruption by the stacking method. Earth Planets Space 68:60. https://doi.org/10.1186/s40623-016-0439-8

Montanaro C, Scheu B, Gudmundsson MT, Vogfjörd K, Reynolds HI, Dürig T, Strehlow K, Rott S, Reuschlé T, Dingwell DB (2016) Multidisciplinary

constraints of hydrothermal explosions based on the 2013 Gengissig lake events, Kverkfjöll volcano, Iceland. Earth Planet Sci Lett 434:308–319. https://doi.org/10.1016/j.epsl.2015.11.043
Murase M, Kimata F, Yamanaka Y, Horikawa S, Matsuhiro K, Matsushima T, Mori H, Ohkura T, Yoshikawa S, Miyajima R, Inoue H, Mishima T, Sonoda T, Uchida K, Yamamoto K, Nakamichi H (2016) Preparatory process preceding the 2014 eruption of Mount Ontake volcano, Japan: insights from precise leveling measurements. Earth Planets Space 68:9. https://doi.org/10.1186/s40623-016-0386-4
Nakajima J, Hasegawa A (2007) Subduction of the Philippine Sea plate beneath southwestern Japan: Slab geometry and its relationship to arc magmatism. J Geophys Res 112:B08306. https://doi.org/10.1029/2006JB004770
Nakamichi H, Kumagai H, Nakano M, Okubo M, Kimata F, Ito Y, Obara K (2009) Source mechanism of a very-long-period event at Mt Ontake, central Japan: response of a hydrothermal system to magma intrusion beneath the summit. J Volcanol Geotherm Res 187(3–4):167–177. https://doi.org/10.1016/j.jvolgeores.2009.09.006
Narita S, Murakami M (2018) Shallow hydrothermal reservoir inferred from post-eruptive deflation at Ontake Volcano as revealed by PALSAR-2 InSAR. Earth Planets Space 70:191. https://doi.org/10.1186/s40623-018-0966-6
Narita S, Murakami M, Tanaka R (2019) Quantitative relationship between plume emission and multiple deflations after the 2014 phreatic eruption at Ontake volcano, Japan. Earth Planets Space 71:145. https://doi.org/10.1186/s40623-019-1124-5
Neidell NS, Taner MT (1971) Semblance and other coherency measures for multichannel data. Geophysics 36(3):482–497. https://doi.org/10.1190/1.1440186
Ogiso M, Matsubayashi H, Yamamoto T (2015) Descent of tremor source locations before the 2014 phreatic eruption of Ontake volcano, Japan. Earth Planets Space 67:206. https://doi.org/10.1186/s40623-015-0376-y
Oikawa T, Yoshimoto M, Nakada S, Maeno F, Komori J, Shimano T, Takeshita Y, Ishizuka Y, Ishimine Y (2016) Reconstruction of the 2014 eruption sequence of Ontake Volcano from recorded images and interviews. Earth Planets Space 68:79. https://doi.org/10.1186/s40623-016-0458-5
Sano Y, Kagoshima T, Takahata N, Nishio Y, Roulleau PDL, Fischer TP (2015) Ten-year helium anomaly prior to the 2014 Mt Ontake eruption. Sci Rep 5:13069. https://doi.org/10.1038/srep13069
Scheu B, Kern H, Spieler O, Dingwell DB (2006) Temperature dependence of elastic P- and S-wave velocities in porous Mt, Unzen dacite. J Volcanol Geotherm Res 153(1–2):136–147. https://doi.org/10.1016/j.jvolgeores.2005.08.007
Stix J, de Moor JM (2018) Understanding and forecasting phreatic eruptions driven by magmatic degassing. Earth Planets Space 70:83. https://doi.org/10.1186/s40623-018-0855-z
Takagi A, Onizawa S (2016) Shallow pressure sources associated with the 2007 and 2014 phreatic eruptions of Mt. Ontake, Japan. Earth Planets Space 68:135. https://doi.org/10.1186/s40623-016-0515-0
Tameguri T, Yakiwara H, Tsutsui T, Iguchi M (2022) High resolution three-dimensional seismic velocity imaging below Aira Caldera. Bull Volcanol Soc Jpn 67(1):69–76. https://doi.org/10.18940/kazan.67.1_69
Tanaka S, Hamaguchi H, Nishimura T, Yamawaki T, Ueki S, Nakamichi H, Tsutsui T, Miyamachi H, Matsuwo N, Oikawa J, Ohminato T, Miyaoka K, Onizawa S, Mori T, Aizawa K (2002) Three-dimensional P-wave velocity structure of Iwate volcano, Japan from active seismic survey. Geophys Res Lett 29(10):59-1–59-4. https://doi.org/10.1029/2002GL014983,2002
Terada A, Kanda W, Ogawa Y, Yamada T, Yamamoto M, Ohkura T, Aoyama H, Tsutsui T, Onizawa S (2021) The 2018 phreatic eruption at Mt. Motoshirane of Kusatsu-Shirane volcano, Japan: eruption and intrusion of hydrothermal fluid observed by a borehole tiltmeter network. Earth Planets Space 73:157. https://doi.org/10.1186/s40623-021-01475-4
Terakawa T, Kato A, Yamanaka Y, Maeda Y, Horikawa S, Matsuhiro K, Okuda T (2016) Monitoring eruption activity using temporal stress changes at Mount Ontake volcano. Nat Commun 7:10797. https://doi.org/10.1038/ncomms10797
Tsukamoto K, Aizawa K, Chiba K, Kanda W, Uyeshima M, Koyama T, Utsugi M, Seki K, Kishita T (2018) Three-dimensional resistivity structure of Iwoyama volcano, Kirishima Volcanic Complex, Japan: relationship to shallow seismicity, surface uplift, and a small phreatic eruption. Geophys Res Lett 45(23):12821–12828. https://doi.org/10.1029/2018GL080202
Ueno H, Hatakeyama S, Aketagawa T, Funasaki J, Hamada N (2002) Improvement of hypocenter determination procedures in the Japan Meteorological Agency. Quart J Seis 65:123–134
Urabe T, Tsukada S (1992) WIN—a workstation program for processing waveform data from microearthquake networks. Prog Abst Seismo Soc Jpn 2:331
Wu S-M, Ward KM, Farrell J, Lin F-C, Karplus M, Smith RB (2017) Anatomy of Old Faithful from subsurface seismic imaging of the Yellowstone Upper Geyser Basin. Geophys Res Lett 44(20):10240–10247. https://doi.org/10.1002/2017GL075255
Yamawaki T, Tanaka S, Ueki S, Hamaguchi H, Nakamichi H, Nishimura T, Oikawa J, Tsutsui T, Nishi K, Shimizu H, Yamaguchi S, Miyamachi H, Yamasato H, Hayashi Y (2004) Three-dimensional P-wave velocity structure of Bandai volcano in northeastern Japan inferred from active seismic survey. J Volcanol Geotherm Res 138(3–4):267–282. https://doi.org/10.1016/j.jvolgeores.2004.07.010
Yukutake Y, Abe Y, Honda R, Sakai S (2021) Magma reservoir and magmatic feeding system beneath Hakone volcano, central Japan, revealed by highly resolved velocity structure. J Geophys Res Solid Earth 126(4):e2020JB021236. https://doi.org/10.1029/2020JB021236

Publisher's Note